

Galectin-3 targeting in thyroid orthotopic tumors opens new ways to characterize thyroid cancer

Francesco De Rose^{1*}, Miriam Braeuer¹, Sten Braesch-Andersen², Angela M. Otto³, Katja Steiger^{4,5}, Sybille Reder¹, Sabine Mall⁶, Stephan Nekolla¹, Markus Schwaiger¹, Wolfgang A. Weber¹, Armando Bartolazzi^{7,8}, Calogero D'Alessandria^{1†}

¹Nuklearmedizinische Klinik und Poliklinik, Klinikum rechts der Isar, Technische Universität München, Ismaninger Str. 22, 81675 München, Germany.

²Mabtech AB Research Laboratory, Nacka Strand, SE-13152, Stockholm, Sweden.

³Munich School of Biomedical Engineering, Technische Universität München, Boltzmannstr. 11, 85748 Garching, Germany.

⁴Institute of Pathology, Klinikum rechts der Isar, Technische Universität München, Ismaninger Str. 22, 81675 München, Germany.

⁵Comparative Experimental Pathology, Klinikum rechts der Isar, Technische Universität München, Ismaninger Str. 22, 81675 München, Germany.

⁶III. Medical Department, Klinikum rechts der Isar, Technische Universität München, Ismaninger Str. 22, 81675 München, Germany.

⁷Pathology Research Laboratory, Cancer Center Karolinska, CCK R8:04, Karolinska Hospital, 17176 Stockholm, Sweden.

⁸Pathology Research Laboratory, Sant'Andrea University Hospital, via di Grottarossa 1035, 00189 Rome, Italy.

† **Corresponding author:** Calogero D'Alessandria, ¹Nuklearmedizinische Klinik und Poliklinik, Klinikum rechts der Isar, Technische Universität München, Ismaninger Str. 22, 81675 München, Germany.

Calogero.dalessandria@tum.de ORCID iD: <https://orcid.org/0000-0003-2381-1212>

* **First author:** Francesco De Rose (PhD student), ¹Nuklearmedizinische Klinik und Poliklinik, Klinikum rechts der Isar, Technische Universität München, Ismaninger Str. 22, 81675 München, Germany.

Francesco.de-rose@tum.de

Key words: Galectin-3; thyroid tumor; PET imaging; ¹²⁴I; orthotopic models.

Running title: New way to characterize thyroid cancer

ABSTRACT

Preoperative characterization of thyroid nodules is challenging since thyroid scintigraphy fails to distinguish between benign and malignant lesions. Galectin-3 (gal-3) is expressed in well-differentiated and in undifferentiated thyroid cancer types but not in normal thyrocytes and benign thyroid lesions. Herein, we aimed to validate gal-3 targeting as a specific method to detect radioiodine non-avid thyroid cancer in thyroid orthotopic tumor models.

Methods Papillary (BcPAP) and anaplastic (CAL62 and FRO82-1) thyroid carcinoma cells lines were characterized via WB and PCR, for gal-3 and sodium-iodide symporter (NIS) expression. A ^{89}Zr -labeled $\text{F(ab}')_2$ anti-gal-3 was generated and characterized for binding versus iodine-125 on 2D and 3D cell cultures. The thyroid carcinoma cells were inoculated into the left thyroid lobe of athymic nude mice, and the orthotopic tumor growth was monitored via ultrasound and fluorescence molecular tomography (FMT). Head-to-head PET/CT comparison of iodine-124 versus ^{89}Zr -DFO- $\text{F(ab}')_2$ anti-gal-3 was performed, followed by biodistribution studies and immunohistochemical analysis for gal-3 and NIS expression.

Results The thyroid carcinoma cells investigated were invariably gal-3 positive, while presenting low/lost NIS expression. ^{89}Zr -DFO- $\text{F(ab}')_2$ anti-gal-3 tracer showed high affinity to gal-3 ($K_d \sim 3.9$ nM) and retained immunoreactivity (>75%) on 2D cell cultures and on tumor spheroids. Iodine-125 internalization in FRO82-1, BcPAP and CAL62 was directly dependent from NIS expression, both in 2D and tumor spheroids. PET/CT imaging showed ^{89}Zr -DFO- $\text{F(ab}')_2$ anti-gal-3 signal associated to the orthotopic-implanted tumors only, while no signal was detected in the tumor-free thyroid lobe. Conversely, PET imaging using iodine-124 showed background accumulation in tumor infiltrated lobe, a condition simulating the presence of radioiodine non-avid thyroid cancer nodules, and high accumulation in normal thyroid lobe. Imaging data were confirmed by tracer biodistribution studies and immunohistochemistry.

Conclusion A specific and selective visualization of thyroid tumor by targeting gal-3 was demonstrated in absence of radioiodine uptake. Translation of this method into clinical setting promises to improve the

management of patients, by avoiding the use of unspecific imaging methodologies and reducing unnecessary thyroid surgery.

INTRODUCTION

Thyroid cancer is the most common endocrine cancer in the US. While the age-adjusted incidence of many cancers has significantly decreased during the last 10 years, a significant increase of thyroid cancer has been reported, with a reported growing cancer incidence rates in men and women since 2005, tripling from 1983 to 2012 (1,2). Since the mortality of thyroid cancer has not changed during the same period of time, and there were no fundamental changes in thyroid cancer therapy, it is generally believed that this marked rise of incidence is caused by an increasing detection of small and clinically insignificant thyroid nodules by ultrasound imaging. To address this “thyroid cancer epidemic”, the criteria for biopsy of thyroid nodules have been revised, and biopsies of small, incidentally detected nodules with morphologically benign features are now discouraged. Furthermore, some thyroid neoplasms (encapsulated follicular neoplasms with papillary features) that were previously classified as malignant are now considered benign (3). These changes have recently led to slowing down of thyroid cancer incidence. However, the clinical criteria for performing biopsies are far from perfect and are mostly based on size of the nodule. Thus, they may also lead to delayed diagnosis of more aggressive thyroid malignancies. While new classifications of thyroid neoplasms on histopathology avoid overtreatment (such as total thyroidectomy, lymph node dissection and radioiodine therapy), it would be preferable if clinically insignificant tumors could be diagnosed prior to surgery.

Differentiation between benign and malignant thyroid nodules is a particular problem in countries with iodine deficiency and a high prevalence of nodular goiter. A combination of ultrasound and thyroid scans with ^{99m}Tc -pertechnetate or ^{123}I are routinely used to characterize thyroid nodules, but their accuracy is limited to multinodular goiter due to reduction or loss of sodium-iodide symporter (NIS) expression in thyroid cancer cells, as result of oncogenic activation (4). Therefore, there is an unmet clinically need for more accurate diagnostic tests to differentiate between benign and malignant thyroid nodules and to characterize thyroid cancer.

Galectin-3 (gal-3) is a well-established histological marker of thyroid cancer that is not expressed by normal thyroid cells. We have previously shown that radiolabeled antibodies directed against gal-3

accumulate in subcutaneous thyroid cancer xenografts in mice and allow for high contrast PET imaging (5,6).

The purpose of this study was to further demonstrate the specificity of thyroid cancer detection by gal-3 targeted antibodies in orthotopic tumor models, characterized by low or lost NIS expression, using PET and fluorescence imaging. We showed that our methodology is highly sensitive in distinguish specifically among normal thyroid tissue and thyroid cancer tissue opening new possibilities for a personalized therapeutic approach to patients affected by thyroid cancer.

MATERIALS AND METHODS

Western Blotting

Cell lysates derived from 2D and 3D cultures of BcPAP (papillary), FO82-1 and CAL62 (anaplastic) were prepared using RIPA buffer and analyzed via western blot as previously reported (6). The following primary antibodies were used: a rat mAb anti-gal-3 (1:5000, M3/38; Mabtech), a mouse mAb anti-NIS (1:500, AB17052; Abcam), a rabbit mAb anti-TTF1 (1:500, 07-60; Millipore) and a mouse mAb anti-GAPDH (1:6000, CB1001; Calbiochem). Gal-3 and TTF-1 were detected via colorimetric method using a goat anti-rat pAb (1:5000, A8438; Sigma) and a goat anti-rabbit mAb (1:5000, AP307A; Millipore) Alkaline Phosphatase (AP)-conjugated secondary antibodies, incubating the blotting membrane with BCIP/NBT chromogen (Abcam) for 5 minutes. The signal corresponding to the hNIS expression was detected using a goat mAb anti-mouse Horseradish Peroxidase (HRP)-conjugated (1:5000, AP124P; Millipore) and chemo-luminescence (ECL kit, Amersham Corporation) by exposing the blotting membrane for 20 minutes to a Hyperfilm ECL (Amersham Corporation). The Amersham ECL Full-Range Rainbow Marker (GE Healthcare) and GAPDH were used as references.

Real-Time Quantitative PCR

To investigate gal-3 and NIS gene expression via PCR analysis, the cDNA was synthesized from total RNA of tumor cell and human thyrocytes (Takara Bio Europe). Primers used for the amplification of

specific sequences are listed in Supplemental Table 1. After the amplification, 10 μ l of each PCR product was separated via electrophoresis on a 1% agarose gel and stained with ethidium bromide. The bands were visualized using an Omega Lum™ C Imaging System (Gel Company). A densitometric analysis of the signals was performed using the ImageJ software, and results were normalized to GAPDH gene.

qPCR was performed using a StepOne Real-Time PCR System (Applied Biosystem, Life technologies) with PowerUp SYBR Green Master Mix (BioRad) and the primers mentioned above. Data were analyzed using the $\Delta\Delta C_t$ method normalizing for the GAPDH C_t value (7).

Probes for Gal-3 Targeting

A $F(ab')_2$ to gal-3 was prepared by pepsin digestion of a full rat mAb to gal-3 (clone M3/38, Mabtech) pre-conditioned as previously reported (8,9).

To perform fluorescence microscopy and fluorescence molecular tomographic (FMT) imaging, the $F(ab')_2$ to gal-3 was conjugated to AlexaFluor®488-TFP dye (GE Healthcare, UK) and to Cy5.5-NHS (GE Healthcare, UK) and the ratios dye/ $F(ab')_2$ to gal-3 were measured via an IMPLEN nanophotometer (IMPLEN, Germany) analyzing samples at specific wavelengths (supplemental data).

For gal-3 immunoPET targeting, the $F(ab')_2$ was functionalized with the chelator desferrioxamine-NCS and labeled with zirconium-89, followed by integrity and stability studies performed as previously described (10,11).

In Vitro Iodine Uptake

Monolayer cell cultures were incubated with 74 kBq of carrier-free ^{125}I -NaI as reported elsewhere (12). BCPAP, CAL62 and FRO82-1 spheroids, produced seeding 150.000, 100.000 and 50.000 cells/well, were incubated for 2 hours with 74 kBq of carrier-free ^{125}I -NaI. Control cell cultures were incubated with 300 μ M $KClO_4$ solution to measure the unspecific iodine uptake. After incubation, spheroids were centrifuged, washed and the pellet-bound activity was counted in a γ -counter.

In Vitro Cell-binding Test of ^{89}Zr -DFO-aGal3-F(ab')₂

Binding affinity of ^{89}Zr -DFO-aGal3-F(ab')₂ and K_d and B_{max} values determination were performed on 2D cell cultures as previously described (6). The immunoreactivity of ^{89}Zr -DFO-aGal3-F(ab')₂ was assessed by Lindmo method (13).

The cellular internalization of ^{89}Zr -DFO-aGal3-F(ab')₂ was studied on 2D cell cultures and by measuring the internalized activity at different time points. Binding to tumor spheroids was tested by incubating spheroids of different cell number with ^{89}Zr -DFO-aGal3-F(ab')₂. Cell-associated activity was counted in gamma-counter.

The binding of aGal3-F(ab')₂ to tumor spheroids was characterized by incubation for 24 hours at 37 °C with AlexaFluor®488-conjugated F(ab')₂ and fluorescent images acquired at different time points using a Biorevo 9000E (Keyence) digital microscope.

Orthotopic Thyroid Cancer Establishment and Monitoring

Six weeks old pathogen-free female athymic Nude-Foxn1^{nu/nu} mice (Charles River Laboratories, Sulzfeld, Germany) were transplanted with thyroid cancer cells as described elsewhere (14), with slight modifications. Establishment of the orthotopic xenograft models and *in vivo* experimental protocols were approved by the local authorities (Regierung von Oberbayern, Germany: license: 55.2-1-54-2532-216-15).

The tumor growth was monitored weekly via ultrasound scan using a Vevo2100 Imaging System (Visualsonics, Toronto, Canada) equipped with a MS550D transducer (40 MHz center frequency, focal depth 4 mm).

The presence of a tumor was confirmed by FMT imaging scan performed 48 hrs post injection of ~54 µg of Cy5.5-labeled aGal3-F(ab')₂ (2 nmol of NIR-dye), using a FMT2500 system (VisEn Medical Inc., Bedford, MA). Image reconstruction and analysis were performed by VisEn FMT™2500 Software.

^{124}I PET/CT Versus ImmunoPET Imaging of Orthotopic Tumors

When the tumors reached 3-5 mm diameter, three groups of mice ($n=3$) bearing the different tumors, were injected *via* catheter in the tail vein with 1.10 ± 0.01 MBq of Iodine-124 (IBA, PerkinElmer) in 300 µl

NaCl 0.9%. One group of healthy mice ($n=3$) injected with same activity were used as control. One hour after injection the animal anesthetized with 5% v/v isoflurane/O₂ underwent 30 minutes PET/CT static acquisition using an Inveon Small Animal PET/CT scanner (Siemens, Knoxville, TN). Characterization of malignant (tumor bearing) versus normal (tumor free) thyroid was performed by immunoPET targeting of gal-3. Two groups of mice per orthotopic tumor type were studied ($n=5$), and two groups of healthy mice ($n=5$ per each tumor) were used as control.

All mice were injected *via* catheter in the tail vein with 2.2 ± 0.2 MBq of ⁸⁹Zr-DFO-aGal3-F(ab')₂ in 250 µl sodium acetate buffer (pH 5.5). 48 hours after tracer injection, mice were anesthetized and imaged via 30 minutes PET/CT static acquisition. Images were reconstructed using OSEM3D/MAP algorithm. Data were normalized and corrected for randoms, dead time and decay with no correction for attenuation or scatter.

Tracer Accumulation Studies

After each imaging session the tracer accumulation in selected organs was measured *ex vivo* as previously described (6) and expressed as percentage of injected dose per gram of tissue (%ID/g).

In vivo tumor uptake of ⁸⁹Zr-DFO-aGal3-F(ab')₂ was analyzed using Inveon Research Workplace software (Siemens, Knoxville, TN). An approximate region of interest (ROI) was drawn on the left thyroid lobe encompassing the tumor signal using a threshold of 50%. The %ID/g was calculated as ratio of mean radioactivity in each ROI (MBq) per gram of tumor (weighted post-mortem) and injected radioactivity (MBq). *In vivo* and *ex vivo* accumulation data were compared for correlation analysis. The right thyroid served as internal control.

A dosimetry study was performed on one group of mice analyzing data of 30 minutes static acquisition at 12, 24, 48 and 70 hours using OLINDA/EXM as described elsewhere (15).

Histology and Immunohistochemistry

Excised tumors were fixed in 10% neutral-buffered formalin solution for 48 h, dehydrated under standard conditions (Leica ASP300S, Wetzlar, Germany) and embedded in paraffin. Serial 3 µm-thin

sections were prepared using a rotary microtome (HM355S, ThermoFisher Scientific, Waltham, USA). Tissue slides were deparaffinized and pretreated with citrate buffer pH 6 for 20 minutes or 30 minutes, for gal-3 and NIS immunostaining. Immunohistochemistry using a primary HRP-conjugated rat mAb anti-gal-3 (Mabtech) or rabbit pAb anti-NIS (Genetex; GTX37599) was performed using a BondMax RXm system (Leica, Wetzlar, Germany). For NIS staining, secondary specie-specific polyclonal antisera with a polymer refine detection kit was applied. Immunoreactivity was visualized with 3,3'-diaminobenzidine for both antibodies. Tumor sections were counterstained with Hematoxylin-Eosin (H.-E.), and normal thyroid tissue served as control. All H.-E.- and immunohistochemical slides were evaluated by certified pathologist blinded for the animal groups. All slides were scanned with a Leica AT2 (Leica, Wetzlar, Germany) system to an e-slide manager database (Leica, Wetzlar, Germany) and evaluated with the Imagescope Software.

Statistical Analyses

Differences in tumor radioactivity uptake between different groups of mice were statistically analyzed with GraphPad Prism 4.0 software using Student's t-test for unpaired data. Two sided significance levels were calculated and $P < 0.05$ $P < 0.01$ values were considered statistically significant.

RESULTS

Gal-3 and hNIS Expression

Monolayer and three-dimensional cultures of BcPAP, FRO82-1 and CAL62 cells showed gal-3 expression, with a band at 31 kDa (Fig. 1A). The relative signal density of gal-3 was ~38% higher in the spheroids than in monolayer cultures (Supplemental Fig. 1A). hNIS expression analysis revealed a band at 68 kDa, which was weaker compared to the gal-3 band but 3-fold stronger for the FRO82-1 and BcPAP than for CAL62 cells (Supplemental Fig. 1A).

A high Gal-3 mRNA expression in 2D cell cultures was detectable compared to normal human thyrocytes, being higher in tumor spheroids. Conversely, hNIS mRNA was undetectable in 2D and 3D cell cultures compared to the expression in normal human thyrocytes (Fig. 1B, Supplemental Fig. 1B,C).

The presence of thyroid transcription factor 1 (TTF-1) double band at 40 kDa confirmed the phenotype of the tumor cell lines (Fig. 1A).

Iodine Uptake in 2D Cell Cultures and Tumor Spheroids

Iodine-125 uptake in monolayer cultures and tumor spheroids was strongly dependent from the differential hNIS expression evidenced via western blot and PCR analysis. Iodine-125 internalization in CAL62 was very low if compared to higher accumulation in FRO82-1 and BcPAP cells (Fig. 2A left). A specular Iodine-125 accumulation was measured on tumor spheroids (Fig. 2A right).

Characterization of Gal-3 Tracers and Cell Binding

Radiolabeling of the anti-gal-3 F(ab')₂ with ⁸⁹Zr provided a probe (⁸⁹Zr-DFO-aGal3-F(ab')₂) with 29.6±2.0 GBq/μmol specific activity, >98% radiochemical purity measured via radio-HPLC (Supplemental Fig. 2A), retained integrity and high stability in human serum (Supplemental Fig. 2B,C).

A K_d of 3.9±0.2 nM and an immunoreactivity of 75.2% (Fig. 2B,C) were measured. In internalization tests, 30% of the added ⁸⁹Zr-DFO-aGal3-F(ab')₂ was internalized after 5 minutes of incubation, reaching

up to 62% (Supplemental Fig. 2D) in the remaining 120 minutes. A size-dependent binding of ^{89}Zr -DFO-aGal3-F(ab')₂ to tumor spheroids was measured (Supplemental Fig. 3A).

A time-dependent penetration of the AlexaFluor488-conjugated probe (5.0 ± 0.1 dye per molecule of F(ab')₂) and a strong fluorescent signal within 5 hours of incubation was evidenced (Fig. 3A), in particular for more compact tumor spheroids (BcPAP and CAL62) compared to cell aggregates (FRO82-1) (Fig. 3B).

The spheroids showed viability and metabolic activity, indirectly measured by the reduction of the water-soluble tetrazolium salt WST-1 (Supplemental Fig. 3B), a reaction catalyzed by cell surface NADH oxidases (16,17). All cell lines showed substantial NOX activity, indicating an active metabolism (18). However, compared to BcPAP and CAL62, the metabolic activity per cell for FRO82-1 spheroid-like structures was about 3-fold higher.

Orthotopic Thyroid Tumor Growth Monitoring

Mice well tolerated the orthotopic transplantation of cancer cells, without any complication related to surgery or anesthesia. BcPAP, FRO82-1 and CAL62 cell lines exhibited high tumorigenicity (>90%) after intra-thyroid injection and a different tumor volume increasing rate with FRO82-1, CAL62 and BcPAP reaching a diameter of 0.3-0.5 cm in 3, 5 and 6 weeks after cell transplantation, respectively.

The growing of tumors was visualized by ultrasound imaging as a small dark area within the left thyroid (Fig. 4A). The neoplastic nature of this structure was confirmed by FMT imaging in the neck region using Cy5.5 conjugated F(ab')₂ to gal-3 (3.6 ± 0.1 dye per molecule of F(ab')₂) (Fig. 4B). The position of the tumor was confirmed at anatomical analysis (Fig. 4C).

Head to Head PET/CT Comparison of Gal-3 Immunotargeting Versus ^{124}I

In control mice injected with ^{124}I -NaI, radioiodine accumulation in both thyroid lobes was visible after 1 hour (Fig. 5, left picture). Control mice injected with ^{89}Zr -DFO-aGal3-F(ab')₂ did not show any accumulation in normal thyroid (Fig. 5, right picture and Supplemental Fig. 4A). Mice bearing tumors showed strong accumulation of ^{124}I in the right thyroid, with a weaker and a decreasing signal in the left

thyroid, for BcPAP>FRO82-1>CAL62, respectively (Fig. 5, left pictures). Conversely, a strong signal associated only to the left thyroid was visible in all mouse models injected with ^{89}Zr -DFO-aGal3-F(ab')₂ (Fig. 5, right pictures, Supplemental Fig. 4B).

In some animal, the enlargement of thyroid lobe during tumor cell injection induced extravasation of medium-containing cells, which infiltrated the neck fatty tissues. Those cells were not visualized via ^{124}I PET/CT, but were highlighted using ^{89}Zr -DFO-aGal3-F(ab')₂.

Tracer Accumulation Analysis

A high Iodine-124 retention was measured in the right thyroid (42.4 ± 5.6 %ID/g) compared to the left thyroid (6.6 ± 2.0 , 2.7 ± 1.1 and 1.7 ± 0.1 %ID/g for BcPAP, FRO82-1 and CAL62 respectively), confirming a reduced tumor NIS expression (Fig. 6A). High accumulation of ^{89}Zr -DFO-aGal3-F(ab')₂ was measured in the left thyroid (7.2 ± 0.9 , 3.9 ± 0.5 and 4.2 ± 1.3 %ID/g, for FRO82-1, BcPAP and CAL62 respectively; Fig. 6B), compared to right thyroid (1.3 ± 0.3 %ID/g).

A low left thyroid/right thyroid Iodine-124 accumulation ratio (0.16 ± 0.02 , 0.06 ± 0.01 and 0.04 ± 0.01) was measured (Supplemental Fig. 5A), compared to ^{89}Zr -DFO-aGal3-F(ab')₂ accumulation ratio (4.0 ± 0.7 , 5.5 ± 1.5 and 3.5 ± 0.9 for BcPAP, FRO82-1 and CAL62 respectively; Supplemental Fig. 5B; Supplemental Table 2, 3) which yield high contrast images. ^{89}Zr -DFO-aGal3-F(ab')₂ retention in liver and spleen can be explained with ^{89}Zr residualization after catabolism of the conjugate (19), while in kidneys is due to tracer excretion (77.0 ± 15.0 %ID/g).

The exposure for the kidneys resulted in an organ dose of 0.01 mSv/MBq, versus an estimated effective total body dose of 0.061 mSv/MBq. A good correlation ($R^2=0.69$) between image-derived uptake calculation and *ex vivo* accumulation analysis was found (Supplemental Fig. 5C).

Immunohistochemical Analysis of Tumor Xenografts and Normal Mouse Thyroid

Immunostaining for NIS expression revealed a stronger signal in BcPAP tumors and a weaker signal for FRO82-1 and a CAL62 (Fig. 7 upper panel, middle insert). Conversely, a high NIS expression was

visualized for the contralateral right thyroid (as expected), with thyrocytes positive for NIS around the thyroidal follicles (Fig. 7 upper panel, right).

Gal-3 expression was detected in the cytoplasm of the thyroid cancer cells infiltrating the left thyroid (Fig. 7 lower panel, middle insert), with a stronger staining for BCPAP and CAL62 tumors compared to FRO82-1. Gal-3 was undetectable in normal residual parenchyma of left thyroid and in the tumor-free right thyroid (Fig. 7 lower panel, right).

DISCUSSION

Thyroid nodules are very common in adults, especially in areas with iodine deficiency. Depending on the ultrasound technology the prevalence in healthy populations ranges between 33% and 68% (20). Currently it is often not possible to exclude a malignant nodule by imaging and fine needle aspiration biopsy, especially in patients with multinodular goiter, because an imaging agent with high and specific uptake in malignant lesions is lacking. This uncertainty results in a large number of thyroidectomies for benign thyroid diseases with a ratio of 1:15 malignant versus benign nodules in Germany, 1:7 in Italy and 1:5 in Great Britain (21). A non-invasive imaging test that specifically accumulates in malignant thyroid nodules could substantially reduce the morbidity from thyroid surgeries for benign nodules and reduce healthcare costs (22).

The specific expression of gal-3 by thyroid cancer makes it an excellent target for the development of such an imaging test (5,6,23,24). In fact, gal-3 staining of thyroid fine needle aspiration (FNA) biopsies has already been shown to be able significantly reduce the number of surgeries for benign thyroid nodules. However, FNA is limited by sampling errors (especially in multinodular goiters) that can be overcome by molecular imaging targeting gal-3. Herein, we therefore performed the preclinical evaluation of gal-3 immunotargeting with ^{89}Zr -DFO-aGal3-F(ab')₂ for detection of malignant thyroid nodules. F(ab)₂ fragments were used because of their faster blood clearance and lower liver uptake than monoclonal antibodies (6,19,25).

We started our evaluation with tumor spheroids, *in vitro* cellular models that better mimic the physiological tissue characteristics (e.g. cell-cell interaction), which help in predicting the *in vivo* results, especially for cell adhesion molecules such as gal-3 (12,26). According to WB and qPCR analysis, the 2D and 3D cell cultures showed low to absent hNIS expression and high gal-3 expression, thus explaining the differential accumulation of ^{125}I on monolayer and spheroids cultures, and the specific binding of ^{89}Zr -DFO-aGal3-F(ab')₂ determined by an active internalization process. The combination of ultrasound and

FMT imaging to monitor the orthotopic tumor growth suggests the possibility to use gal-3 specific probes conjugated to NIR-dye (700-900 nm) for performing image-guided surgery of thyroid nodules (27-29).

The head-to-head comparison of ^{124}I PET/CT versus galectin-3 targeting demonstrated the specificity of our methodology for thyroid cancer imaging. High uptake of ^{89}Zr -DFO-aGal3-F(ab')₂ was observed for the orthotopic thyroid tumors that showed only minimal or no radioiodine uptake. Conversely, the normal thyroid demonstrated high radioiodine uptake, but no specific uptake of ^{89}Zr -DFO-aGal3-F(ab')₂. These imaging findings were confirmed by *ex vivo* biodistribution studies for ^{89}Zr -DFO-aGal3-F(ab')₂. Lack of ^{89}Zr -DFO-aGal3-F(ab')₂ uptake by the normal thyroid tissue is not due to species differences since the F(ab')₂ recognizes an amino-terminal common epitope of human and mouse gal-3 (23,24).

The high uptake of ^{89}Zr -DFO-aGal3-F(ab')₂ in thyroid tumors without significant radioiodine uptake also indicates that gal-3 is a promising target for staging and potentially radionuclide therapy of radioiodine negative or refractory thyroid cancer. The high kidney uptake of ^{89}Zr -DFO-aGal3-F(ab')₂ is a limitation for therapeutic applications. However, it may be reduced by co-administration of cationic amino acids solutions or basic polypeptides (poly-lysine) (30). In addition, modifications of antibody fragments by PEGylation have been shown to drastically reduce renal uptake (31).

CONCLUSION

In conclusion, using an anti-gal3 F(ab')₂ we hereby demonstrated that molecular imaging of gal-3 expression is a new tool for *in vivo* detection of thyroid cancer. Our results are promising for non-invasive identification of malignant thyroid nodules with nuclear and optical imaging, staging of thyroid cancer, as well as targeted radionuclide therapy of metastatic, radioiodine negative thyroid cancer.

ACKNOWLEDGMENTS

The authors thank: Michael Kuhlmann from the EIMI of Westfälische-Wilhelms-Universität in Münster for teaching with intrathyroidal tumor cell implantation; Markus Mittelhäuser for animal tracer injection; Marion Mielke for supporting with tissue immunostaining; Joseph Hintermair for helping with spheroids establishment and WST-1 analysis; Stephanie Rämisch for RNA isolation assistance. This study was funded by Deutsche Forschungsgemeinschaft (grant number: DA 1552/2-1), SFB824 (Z2) and SFB824 (C10).

REFERENCES

1. Morris LG, Tuttle RM, Davies L. Changing Trends in the Incidence of Thyroid Cancer in the United States. *JAMA Otolaryngol Head Neck Surg.* 2016;142:709-711.
2. Siegel RL, Miller KD, Jemal A. Cancer statistics, 2018. *CA Cancer J Clin.* 2018;68:7-30.
3. Nikiforov YE, Seethala RR, Tallini G, et al. Nomenclature Revision for Encapsulated Follicular Variant of Papillary Thyroid Carcinoma: A Paradigm Shift to Reduce Overtreatment of Indolent Tumors. *JAMA Oncol.* 2016;2:1023-1029.
4. Kogai T, Brent GA. The sodium iodide symporter (NIS): regulation and approaches to targeting for cancer therapeutics. *Pharmacol Ther.* 2012;135:355-370.
5. Bartolazzi A, D'Alessandria C, Parisella MG, et al. Thyroid cancer imaging in vivo by targeting the anti-apoptotic molecule galectin-3. *PLoS One.* 2008;3:e3768.
6. D'Alessandria C, Braesch-Andersen S, Bejo K, et al. Noninvasive In Vivo Imaging and Biologic Characterization of Thyroid Tumors by ImmunoPET Targeting of Galectin-3. *Cancer Res.* 2016;76:3583-3592.
7. Livak KJ, Schmittgen TD. Analysis of relative gene expression data using real-time quantitative PCR and the 2^{(-Delta Delta C(T))} Method. *Methods.* 2001;25:402-408.
8. Rousseaux J, Rousseaux-Prevost R, Bazin H. Optimal conditions for the preparation of Fab and F(ab')₂ fragments from monoclonal IgG of different rat IgG subclasses. *J Immunol Methods.* 1983;64:141-146.
9. Inohara H, Raz A. Functional evidence that cell surface galectin-3 mediates homotypic cell adhesion. *Cancer Res.* 1995;55:3267-3271.
10. Yusufi N, Mall S, Bianchi HO, et al. In-depth Characterization of a TCR-specific Tracer for Sensitive Detection of Tumor-directed Transgenic T Cells by Immuno-PET. *Theranostics.* 2017;7:2402-2416.
11. Sham JG, Kievit FM, Grierson JR, et al. Glypican-3-targeted 89Zr PET imaging of hepatocellular carcinoma. *J Nucl Med.* 2014;55:799-804.
12. Singh TD, Jeong SY, Lee SW, et al. Inverse Agonist of Estrogen-Related Receptor gamma Enhances Sodium Iodide Symporter Function Through Mitogen-Activated Protein Kinase Signaling in Anaplastic Thyroid Cancer Cells. *J Nucl Med.* 2015;56:1690-1696.

13. Lindmo T BE, Cuttitta F, Fedorko J, Bunn PA Jr. Determination of the immunoreactive fraction of radiolabeled monoclonal antibodies by linear extrapolation to binding at infinite antigen excess. *J Immunol Methods*. 1984;72:77-89.
14. Buther K, Compeer MG, De Mey JG, et al. Assessment of endothelin-A receptor expression in subcutaneous and orthotopic thyroid carcinoma xenografts in vivo employing optical imaging methods. *Endocrinology*. 2012;153:2907-2918.
15. Stabin MG, Sparks RB, Crowe E. OLINDA/EXM: the second-generation personal computer software for internal dose assessment in nuclear medicine. *J Nucl Med*. 2005;46:1023-1027.
16. Otto AM, Paddenberg R, Schubert S, Mannherz HG. Cell-cycle arrest, micronucleus formation, and cell death in growth inhibition of MCF-7 breast cancer cells by tamoxifen and cisplatin. *J Cancer Res Clin Oncol*. 1996;122:603-612.
17. Berridge MV, Herst PM, Tan AS. Tetrazolium dyes as tools in cell biology: new insights into their cellular reduction. *Biotechnol Annu Rev*. 2005;11:127-152.
18. Otto AM, Hintermair J, Janzon C. NADH-linked metabolic plasticity of MCF-7 breast cancer cells surviving in a nutrient-deprived microenvironment. *J Cell Biochem*. 2015;116:822-835.
19. Anderson CJ, Connett JM, Schwarz SW, et al. Copper-64-labeled antibodies for PET imaging. *J Nucl Med*. 1992;33:1685-1691.
20. Guth S, Theune U, Aberle J, Galach A, Bamberger CM. Very high prevalence of thyroid nodules detected by high frequency (13 MHz) ultrasound examination. *Eur J Clin Invest*. 2009;39:699-706.
21. Rosato L, Avenia N, Bernante P, et al. Complications of thyroid surgery: analysis of a multicentric study on 14,934 patients operated on in Italy over 5 years. *World J Surg*. 2004;28:271-276.
22. Scott-Combes D, Kinsman R. *The British Association of Endocrine Surgeons: Second National Audit Report 2007*. Oxfordshire, United Kingdom: Dendrite Clinical Systems Ltd; 2007.
23. Bartolazzi A, Gasbarri A, Papotti M, et al. Application of an immunodiagnostic method for improving preoperative diagnosis of nodular thyroid lesions. *Lancet*. 2001;357:1644-1650.
24. Bartolazzi A, Orlandi F, Saggiorato E, et al. Galectin-3-expression analysis in the surgical selection of follicular thyroid nodules with indeterminate fine-needle aspiration cytology: a prospective multicenter study. *Lancet Oncol*. 2008;9:543-549.

25. Sham JG, Kievit FM, Grierson JR, et al. Glypican-3-targeting F(ab')₂ for 89Zr PET of hepatocellular carcinoma. *J Nucl Med*. 2014;55:2032-2037.
26. Fortunati N, Catalano MG, Arena K, Brignardello E, Piovesan A, Boccuzzi G. Valproic acid induces the expression of the Na⁺/I⁻ symporter and iodine uptake in poorly differentiated thyroid cancer cells. *J Clin Endocrinol Metab*. 2004;89:1006-1009.
27. Li Y, Li Z, Wang X, et al. In vivo cancer targeting and imaging-guided surgery with near infrared-emitting quantum dot bioconjugates. *Theranostics*. 2012;2:769-776.
28. Kahramangil B, Berber E. The use of near-infrared fluorescence imaging in endocrine surgical procedures. *J Surg Oncol*. 2017;115:848-855.
29. Vahrmeijer AL, Hutteman M, van der Vorst JR, van de Velde CJ, Frangioni JV. Image-guided cancer surgery using near-infrared fluorescence. *Nat Rev Clin Oncol*. 2013;10:507-518.
30. Behr TM, Goldenberg DM, Becker W. Reducing the renal uptake of radiolabeled antibody fragments and peptides for diagnosis and therapy: present status, future prospects and limitations. *Eur J Nucl Med*. 1998;25:201-212.
31. Rashidian M, Ingram JR, Dougan M, et al. Predicting the response to CTLA-4 blockade by longitudinal noninvasive monitoring of CD8 T cells. *J Exp Med*. 2017;214:2243-2255.

Figures

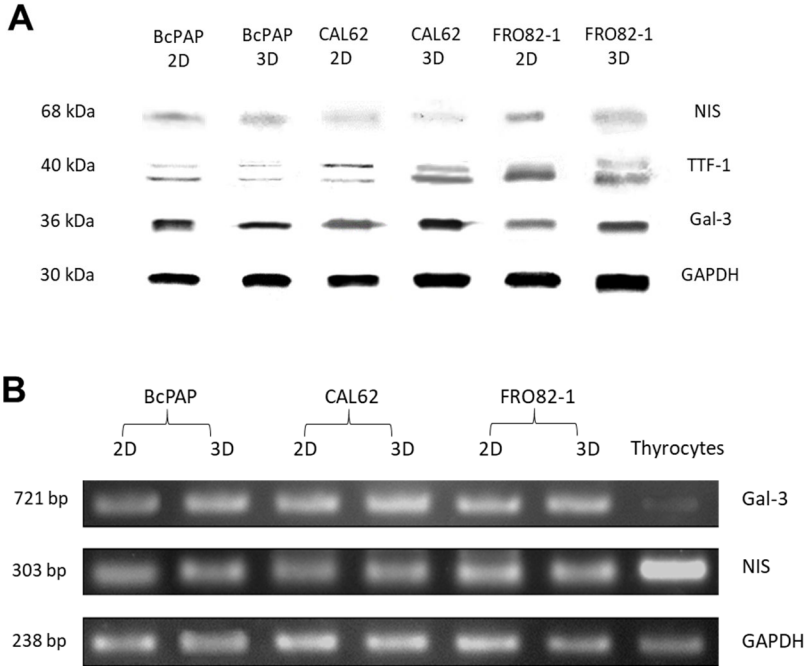


FIGURE 1: 2D and 3D cell cultures characterization. **(A)** Cell lysates from monolayer (2D) and spheroids (3D) cell cultures analyzed via western blot. Bands separation was performed with a 100V voltage for 90 minutes. **(B)** Electrophoretic separation of cDNA encoding for gal-3 and hNIS on 1% agarose gel, using a voltage of 80V for 60 minutes, and staining with ethidium bromide.

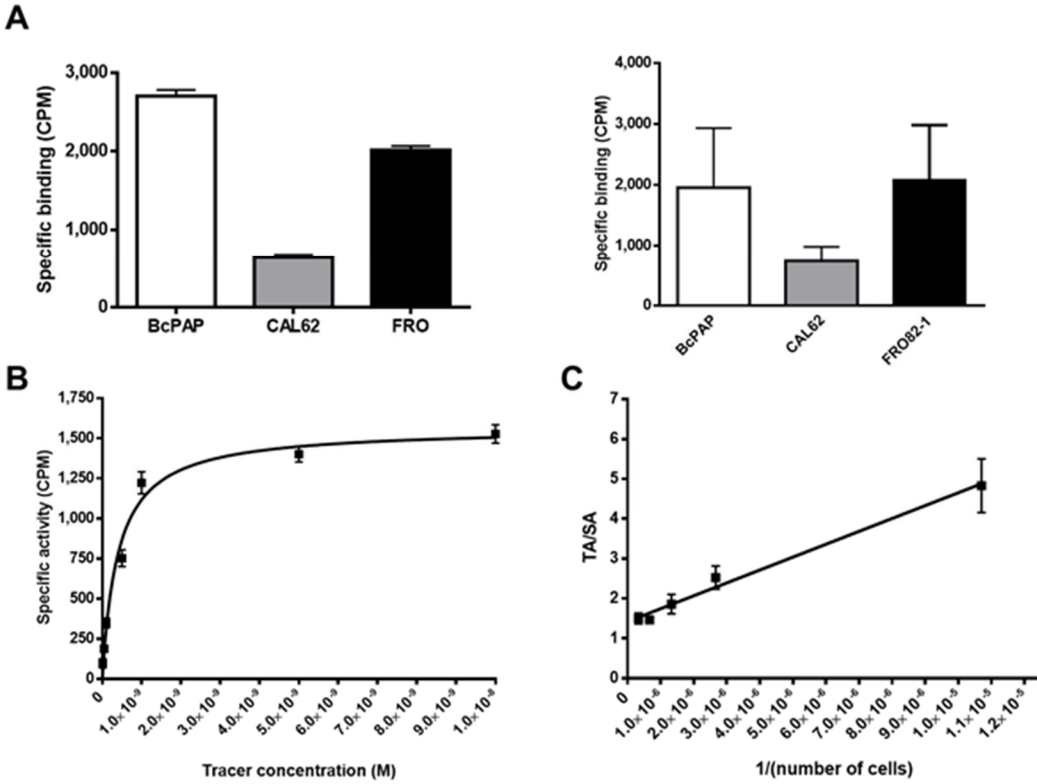


FIGURE 2. Iodine-125 and ^{89}Zr -Df-aGal3-F(ab')₂ cell binding analysis. **(A)** Iodine-125 uptake assay performed on 2D (left) and 3D (right) cell cultures. **(B)** Binding affinity test of ^{89}Zr -Df-aGal3-F(ab')₂ on 2D cells incubated with increasing concentration of tracer and **(C)** immunoreactivity assessed on cells dilutions from 6.0×10^6 to 1×10^5 incubated with a constant concentration of tracer. Data representative of three independent experiments performed each time in triplicate, and are expressed as mean \pm SD.

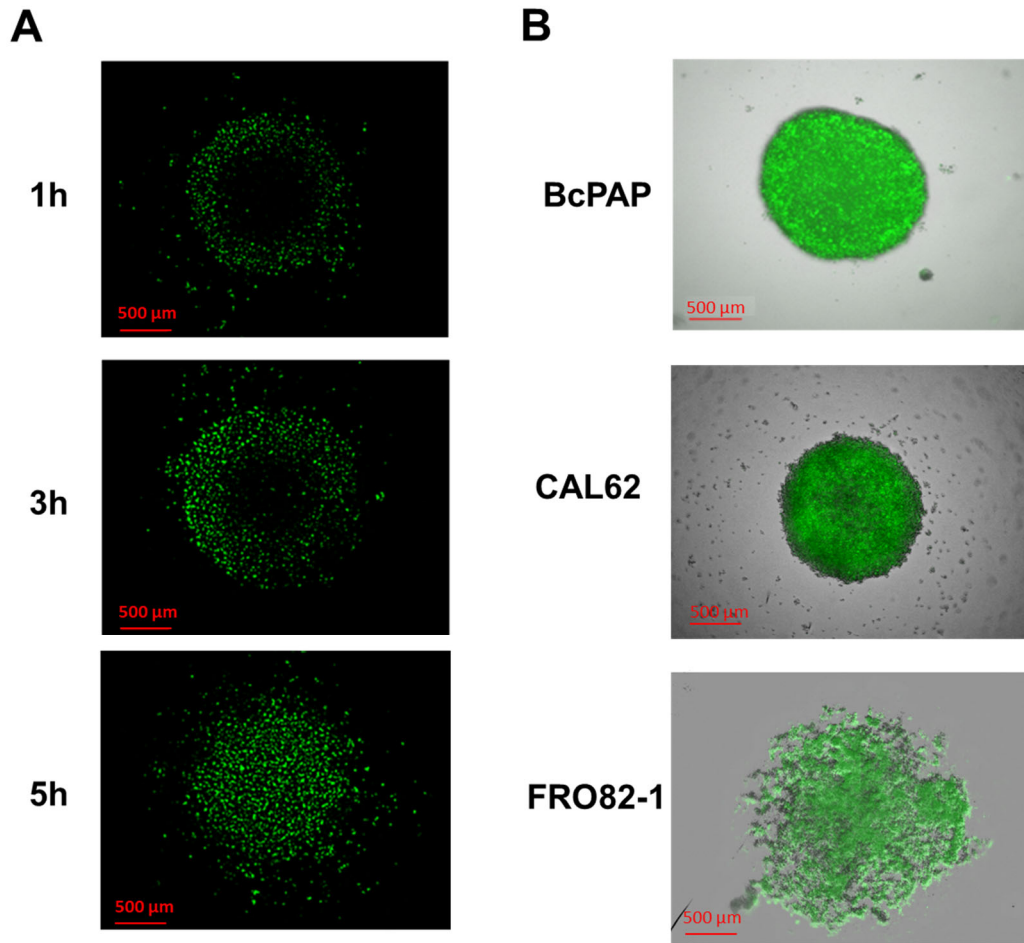


FIGURE 3: Characterization of gal-3-specific F(ab')₂ binding to spheroids. **(A)** Time dependent penetration of AlexaFluor488-aGal3-F(ab')₂ into BcPAP tumor spheroids during incubation with 10 μg/ml AlexaFluor488-conjugate (representative image). **(B)** Full focus confocal and fluorescent overlay of tumor spheroids.

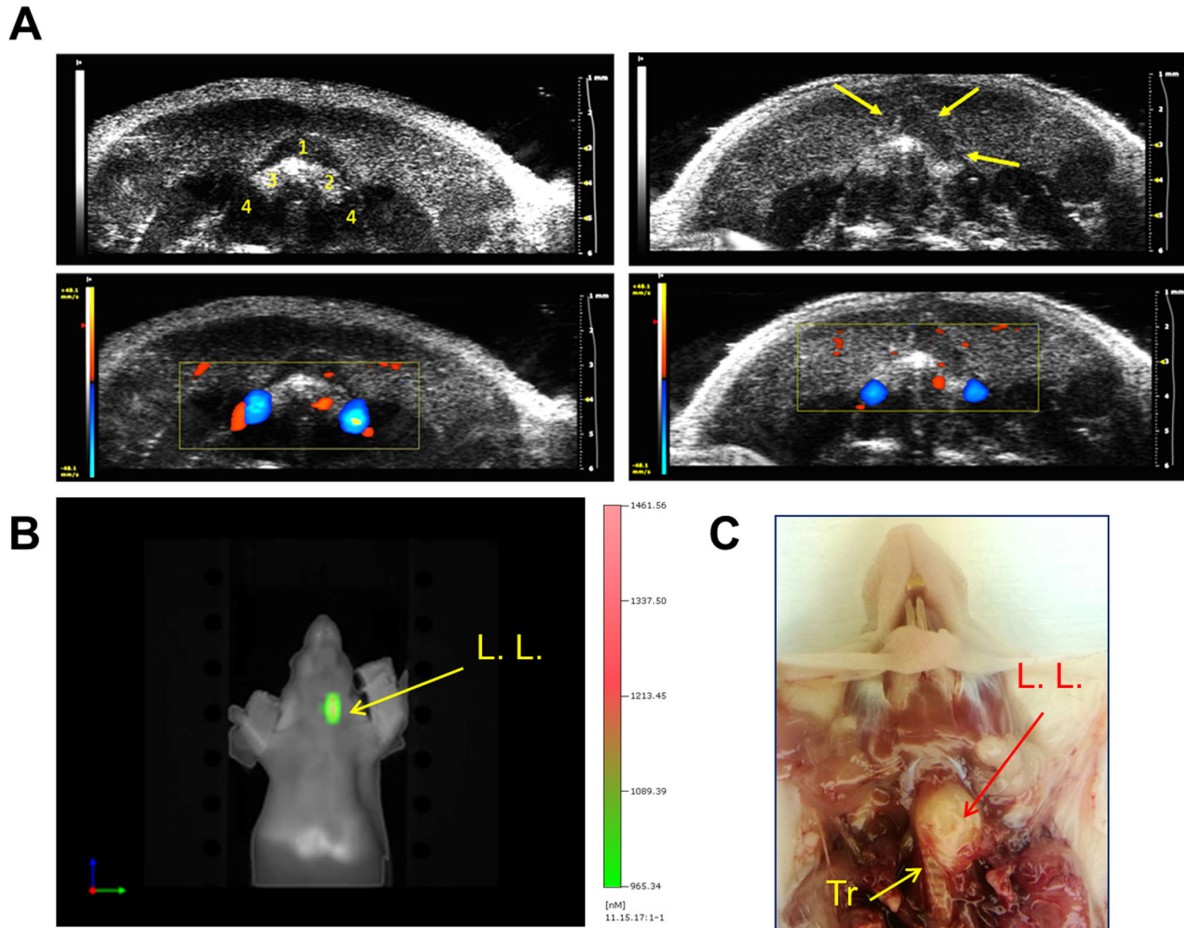


FIGURE 4. Orthotopic tumor growth monitoring. (A) Above: representative ultrasound transversal image of a mouse neck before thyroid cancer cell transplantation (left): 1) strap muscle; 2) left thyroid lobe; 3) right thyroid lobe; 4) carotid arteries. On the right, ultrasound image showing the orthotopic tumor (yellow arrows) expanding from the left lobe. Below: “Doppler mode” acquisition enhances the activity of carotid arteries and allows correct finding of the thyroid. (B) FMT imaging of the same mouse performed 48 hours after injection of Cy5.5-labeled aGal3-F(ab’)₂ and visualizing a gal-3 positive mass in the neck. (C) Anatomical analysis of thyroid orthotopic tumor at necropsy. (Tr= trachea; L.L.= left lobe).

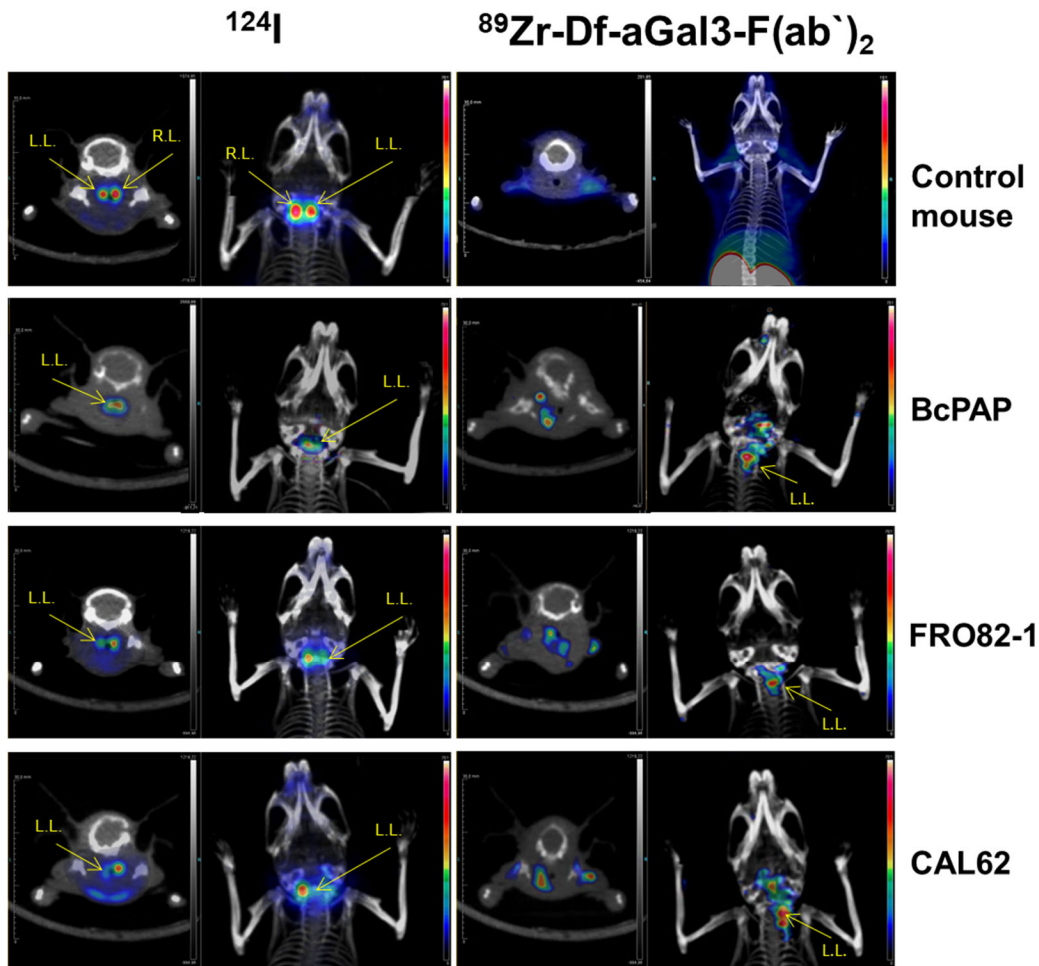


FIGURE 5: Head-to-head comparison of ^{124}I versus ^{89}Zr -DFO-aGal3-F(ab')₂ detection of thyroid orthotopic tumors. Representative μPET images acquired 1 hour post injection of Iodine-124 and 48 hours post injection of ^{89}Zr -DFO-aGal3-F(ab')₂. Each row presents the axial PET/CT fusion projection and 3D projection for both tracers.

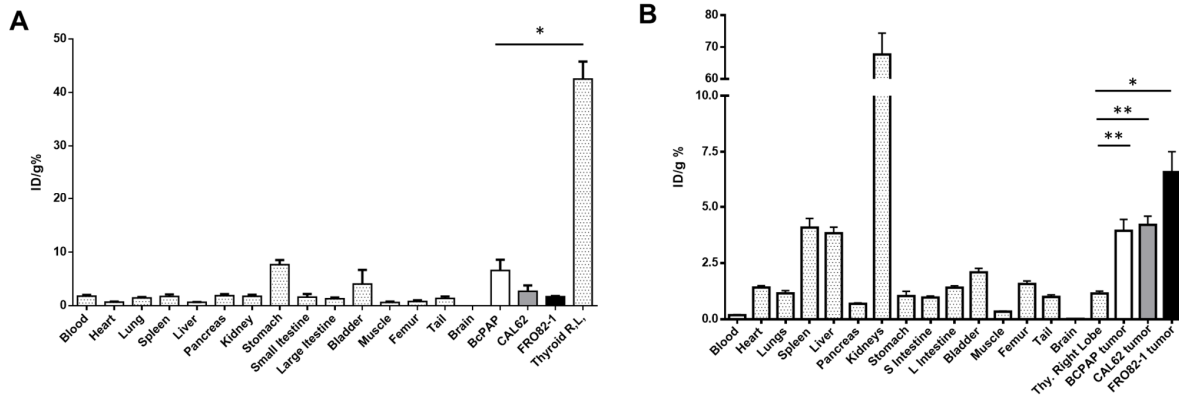


FIGURE 6: Biodistribution analysis of ^{124}I versus ^{89}Zr -DFO-aGal3-F(ab')₂. Three groups of mice ($n=3$ /tumor type) were injected with iodine-124 and two groups of mice ($n=5$) per each type of tumor were injected with ^{89}Zr -DFO-aGal3-F(ab')₂. **(A)** Low NIS expression in orthotopic tumors yielded in a low ^{124}I accumulation in the left lobe compared to the right lobe (R.L.). Differences were statistically significant (* $p<0.01$). **(B)** A strong ^{89}Zr -DFO-aGal3-F(ab')₂ retention was measured in orthotopic tumors, with background accumulation in the right lobes. Differences in ^{89}Zr -DFO-aGal3-F(ab')₂ accumulation were statistically significant (* $p<0.01$ for FRO82-1, ** $p<0.05$ for BcPAP and CAL62).

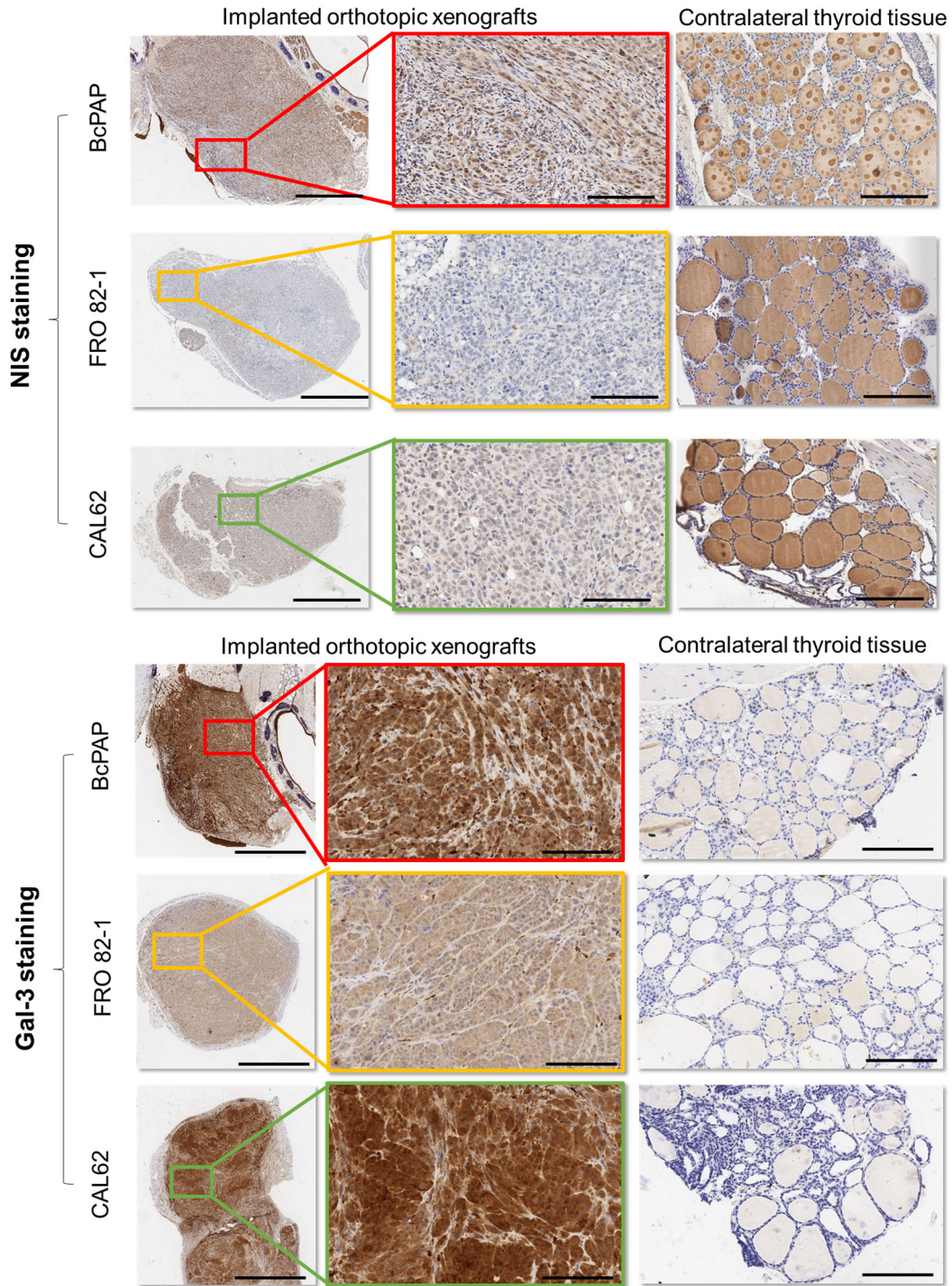


FIGURE 7: Immunohistochemical analysis for NIS and gal-3 expression. Tissue sections derived from normal and tumor infiltrated thyroid lobes were stained for NIS and gal-3 expression using a rabbit

polyclonal antibody anti-NIS (0.5 mg/ml; Genetex, GTX37599) and an HRP-conjugated rat mAb to gal-3 (Mabtech) (10 µg/ml). Upper panel, the middle insert shows the weak membrane staining on tumor cells and (right) normal lobe with thyreocytes positive for NIS staining. Lower panel reports Gal-3 staining. The middle insert shows cytoplasmic staining, and (right) normal lobe without any visible signal for gal-3. (Magnification: left 4X (bar code 2.0 mm), insert middle 20X (bar code 300 µm); right 10X (bar code 1 mm)).

Galectin-3 immunotargeting in thyroid orthotopic tumors opens new ways for *in vivo* thyroid cancer characterization and therapy decision making

De Rose F¹, Braeuer M¹, Braesch-Andersen S², Reder S¹, Otto AM³,
Katja S^{4,5}, Mall S⁶, Nekolla S¹, Schwaiger M¹, Wolfgang
A. Weber¹, Bartolazzi A^{7,8}, D'Alessandria C^{1*}

¹Nuklearmedizinische Klinik und Poliklinik, Klinikum rechts der Isar, Technische Universität München, Ismaninger Str. 22, 81675 München, Germany.

²Mabtech AB Research Laboratory, Nacka Strand, SE-13152, Stockholm, Sweden.

³Munich School of Biomedical Engineering, Technische Universität München, Boltzmannstr. 11, 85748 Garching, Germany.

⁴Institute of Pathology, Klinikum rechts der Isar, Technische Universität München, Ismaninger Str. 22, 81675 München, Germany.

⁵Comparative Experimental Pathology, Klinikum rechts der Isar, Technische Universität München, Ismaninger Str. 22, 81675 München, German.

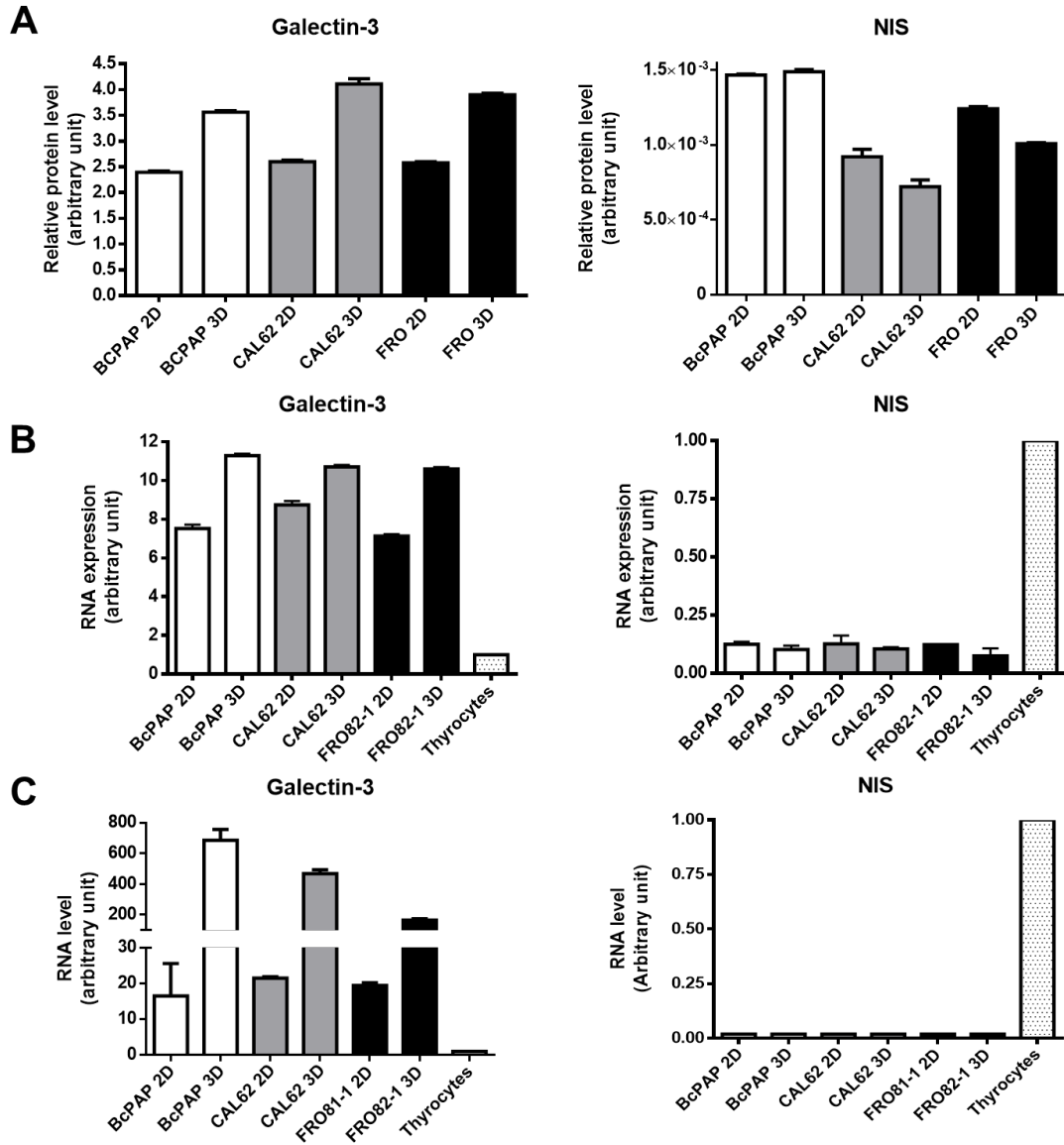
⁶III. Medical Department, Klinikum rechts der Isar, Technische Universität München, Germany.

⁷Pathology Research Laboratory, Cancer Center Karolinska, CCK R8:04, Karolinska Hospital, 17176 Stockholm, Sweden.

⁸Pathology Research Laboratory, Sant'Andrea University Hospital, via di Grottarossa 1035, 00189 Rome, Italy.

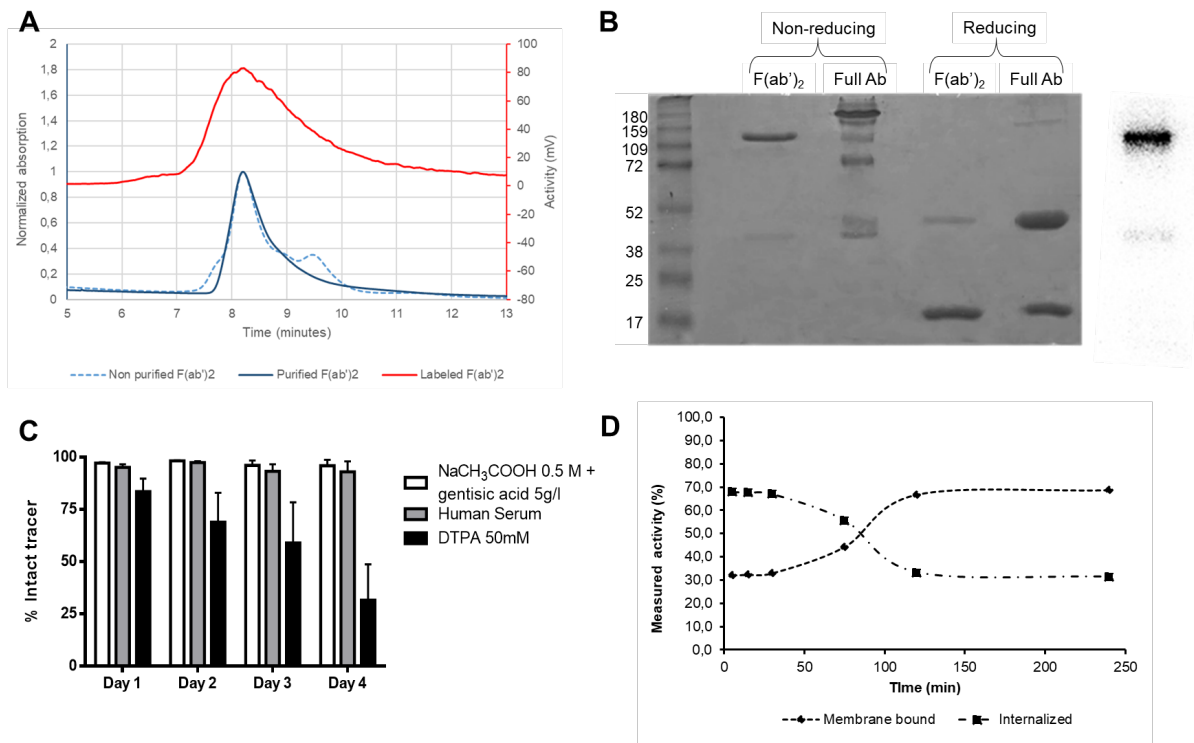
Supplemental Figures and Tables

Supplemental Figure 1



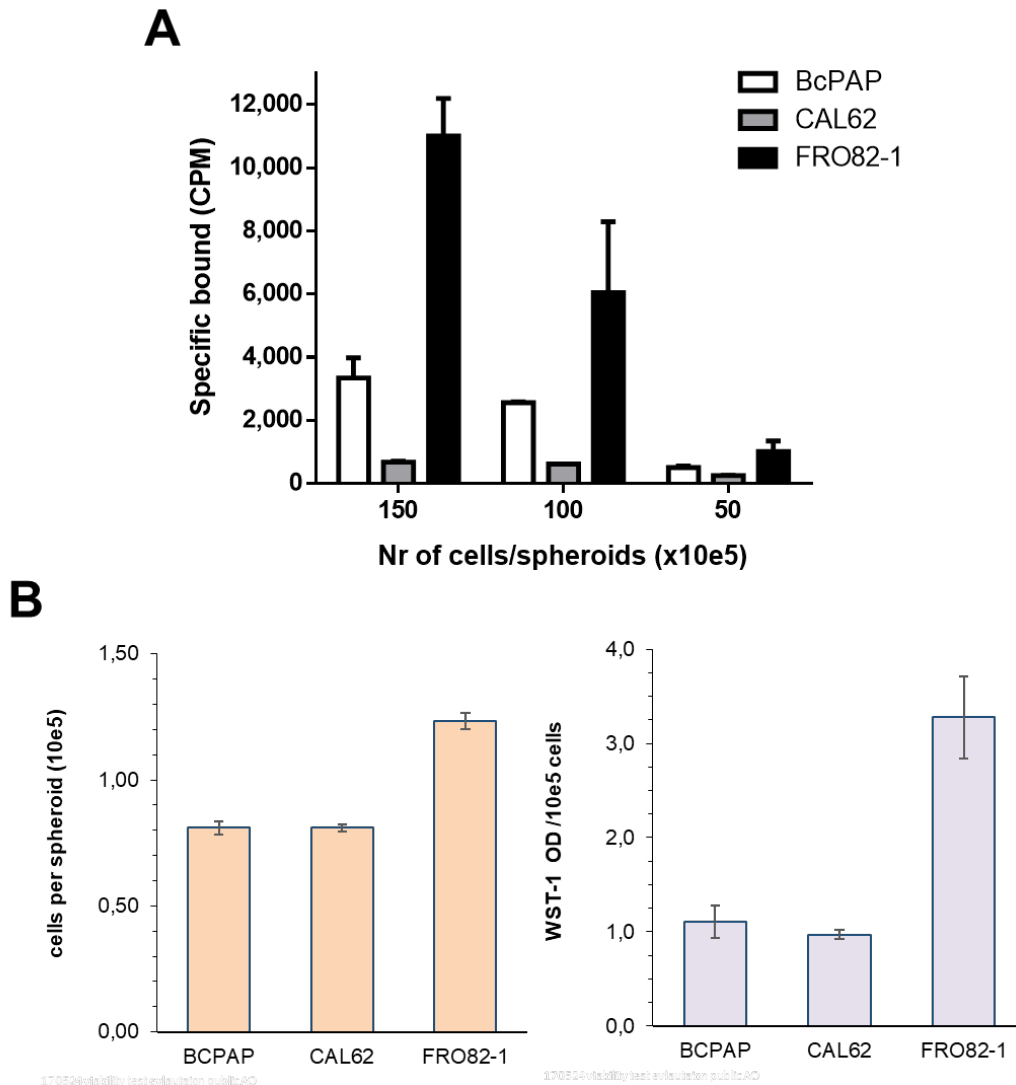
Supplemental Figure 1. Characterization of Gal-3 and NIS expression in the selected cell lines. **(A)** Relative densitometric analysis of bands visualized for gal-3 and NIS expression via western blot normalizing for the signal related to GADPH. **(B)** Relative intensity measurement of the bands visualized for cDNA sequences encoding for Gal-3 and NIS analyzed via PCR. WB and PCR analysis were repeated at least 5 times, each test in triplicate. **(C)** Gal-3 and hNIS gene expression analysis evaluated via qPCR on cDNA derived from total RNA extracted from 2D and 3D cell cultures. Total RNA extract from human thyrocytes (Takara Bio Europe) was used as reference. Data from qPCR were analyzed using $\Delta\Delta C_t$ method.

Supplemental Figure 2



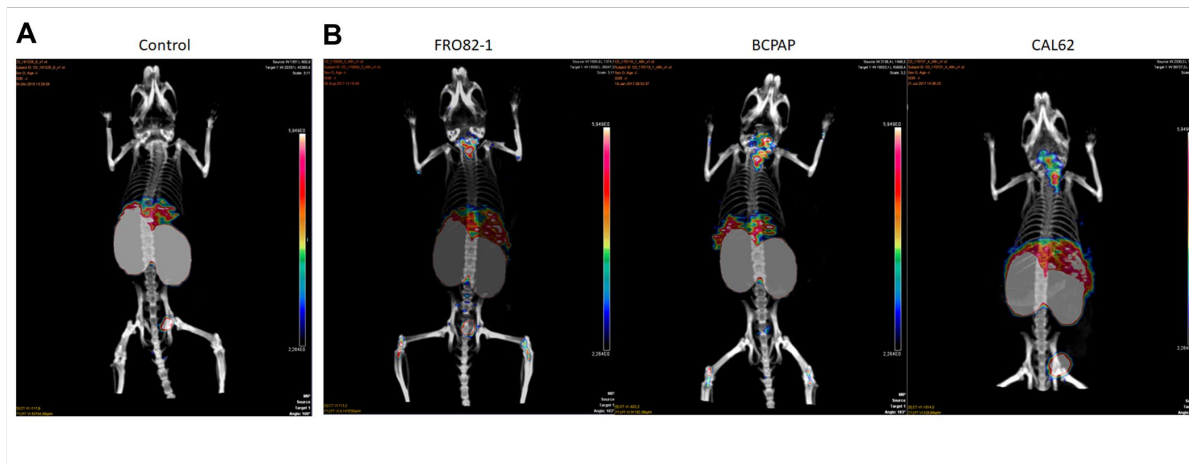
Supplemental Figure 2. *In vitro* characterization of ⁸⁹Zr-DFO-aGal3-F(ab')₂ tracer. **(A)** The radiochemical purity measured via radio-HPLC analysis was > 98%, with radioactivity associated with the peak of F(ab')₂ (t_R= 8.3 min.) in UV profile. **(B)** The integrity of the F(ab')₂ to gal-3 after conjugation and radiolabeling was confirmed via SDS-PAGE carried out under reducing and non-reducing condition, followed by and autoradiography analysis of the radiolabeled F(ab')₂. **(C)** The stability of ⁸⁹Zr-labelled F(ab')₂ to gal-3 in different storage solutions were tested. Aliquots of ⁸⁹Zr-DFO-aGal3-F(ab')₂ probe (1 μl) were taken from each storage solution at different time point, spotted onto a TLC silica gel strip and developed using 0.02 M citrate buffer with 50mM DTPA (pH 5.0) as solvent. ⁸⁹Zr-labelled F(ab')₂ to gal-3 was incubated in 50 mM DTPA solution to determine transchelation effect. Analysis were repeated at least three times, each time in triplicate. Data are presented as mean±SD. **(D)** Internalization test of ⁸⁹Zr-DFO-aGal3-F(ab')₂ on 2D cultures. Membrane bound and internalized activity measured at different time points.

Supplemental Figure 3



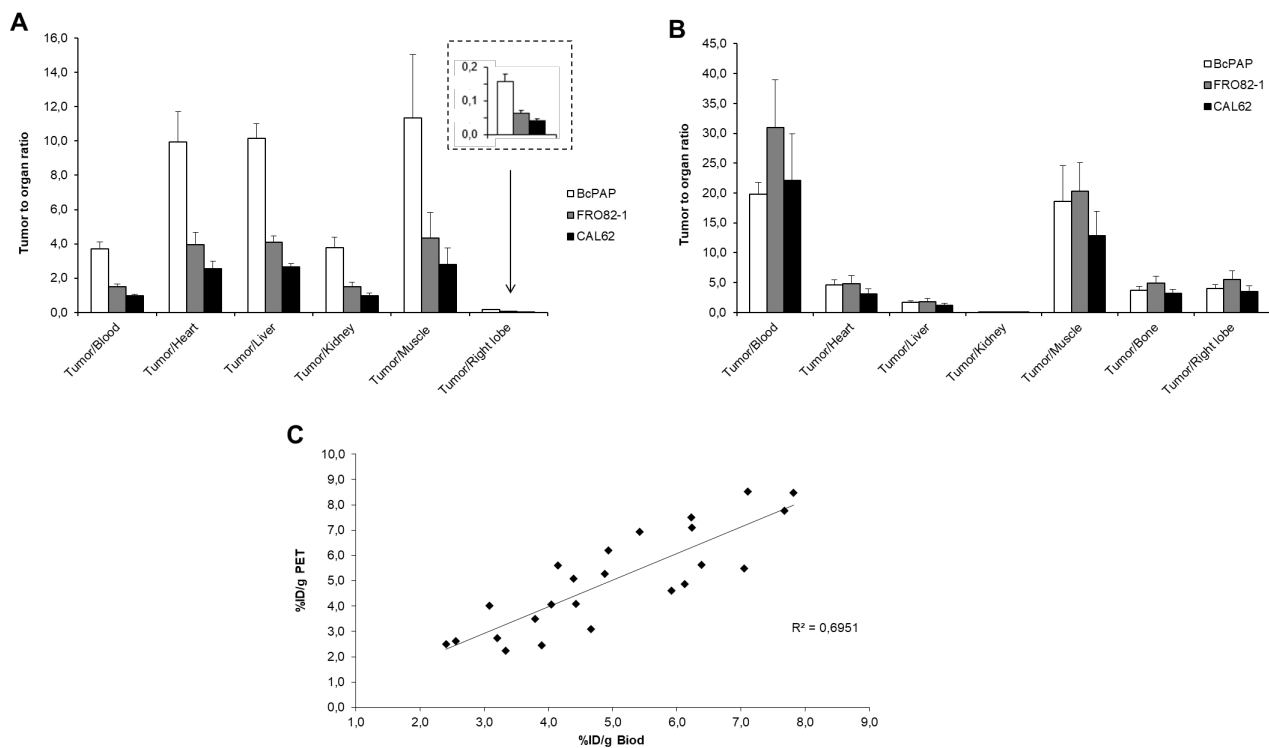
Supplemental Figure 3. Binding and viability tests on tumor spheroids. (A) ^{89}Zr -DFO-aGal3-F(ab')₂ binding on 3D tumor spheroids, assessed in presence or absence of excess of aGal3-F(ab')₂ to evaluate unspecific binding. Data representative of three independent experiments performed each time in triplicate and are expressed as mean±SD. (B) Number of cells counted (x100k) per spheroids/aggregates after three days of incubation of 10e5 cells under non-adhesive conditions (upper graph). Metabolic activity evaluated via WST-1 reduction measured as OD450nm-OD630nm (lower graph).

Supplemental Figure 4



Supplemental Figure 4. In vivo ^{89}Zr -DFO-F(ab')₂ to gal-3 tumor accumulation. Maximum Imaging Projection (MIP) images of static PET/CT scans acquired at 48h post injection of 2.22 MBq (60 μCi) ^{89}Zr -DFO-aGal3-F(ab')₂. (A) No specific tracer accumulation was present in the neck region in healthy control mice, (B) vice versa, high tumor to background contrast in the region of neck is showed in each orthotopic model with detailed information about tumor position. Images were analyzed using Inveon Research Workplace software (Siemens, Knoxville, TN).

Supplemental Figure 5



Supplemental Figure 5. Biodistribution analysis of ^{124}I versus ^{89}Zr -DFO-aGal3-F(ab')₂. ^{124}I (A) and ^{89}Zr -DFO-aGal3-F(ab')₂ (B) accumulation ratio in left lobe/right lobe. Radioactivity accumulation was calculated as mean \pm SD. (C) *In vivo* versus *ex vivo* ^{89}Zr -DFO-F(ab')₂ to gal-3 tumor accumulation analysis. Image-derived uptake calculation and *ex vivo* accumulation analyses were compared for all the mice investigated in this work. For *in vivo* tumor uptake analysis, images were analyzed using Inveon Research Workplace software (Siemens, Knoxville, TN). An arbitrary regions of interest (ROI) was drawn manually on the left side of the trachea encompassing the tumor signal. The radioactivity present in each ROI was determined using a threshold of 50%. The %ID/g was calculated as a ratio of mean radioactivity in each ROI (MBq) per gram of tumor tissue (weighted post-mortem) and radioactivity (MBq) injected in the whole body. *Ex vivo* accumulation data were obtained from biodistribution studies by counting the tumors in γ -counter. A correlation equal to $R^2=0.69$ was found between the two tracer accumulation analysis. Ten mice per each group were analyzed using both approaches. Data are presented without taking into account the tumor type analyzed.

Supplemental Tables

Gene	Sequence 5'-3'
GAPDH	Sense: GAGTCAACGGATTTGGTCGT Antisense: TTGATTTTGGAGGGATCTCG
NIS	Sense: CTGCCCCAGACCAGTACATGCC Antisense: TGACGGTGAAGGAGCCCTGAAG
Gal-3	Sense: GCCTCGCATGCTGATAACAA Antisense: ACCGACTGTCTTTCTTCCT

Supplemental Table 1. Primers used for Gal-3 and hNIS gene expression analysis via qPCR. GAPDH was used as housekeeping genes.

Tumor/organ ratio	BcPAP (n = 10)	FRO82-1 (n = 10)	CAL62 (n = 10)
Tumor/blood	3.71 ± 0.40	1.51 ± 0.16	0.97 ± 0.10
Tumor/heart	9.93 ± 1.78	4.04 ± 0.72	2.59 ± 0.46
Tumor/liver	10.16 ± 0.85	4.13 ± 0.35	2.65 ± 0.22
Tumor/kidney	3.77 ± 0.60	1.53 ± 0.24	0,99 ± 0.16
Tumor/muscle	11.34 ± 3.70	4.61 ± 1.50	2.96 ± 0.97
Left/Right lobe	0.16 ± 0.02	0.06 ± 0.01	0.04 ± 0.01

Supplemental Table 2. Tumor/organs accumulation ratio analysis for ^{124}I in thyroid orthotopic models. The tumor-to-organ ratio values were calculated from γ -counter measurements of selected organs analyzed at 1hr after ^{124}I injection. A positive tumor/organ ratio was measured for all selected organs. A very low left/right lobe ratio was measured for all models investigated, due to the low accumulation of ^{124}I in the tumor bearing left lobe compared to the right normal thyroid lobe. These results correlate well with the very low NIS expression found out in western blot and PCR analysis. Data are expressed as mean %ID/g \pm SD.

Tumor/organ ratio	BcPAP (n = 10)	FRO82-1 (n = 10)	CAL62 (n = 10)
Tumor/blood	19.77 ± 1.95	30.99 ± 7.96	22.14 ± 7.82
Tumor/heart	4.65± 0.81	4.79± 1.43	3.05± 0.89
Tumor/liver	1.69± 0.24	1.84± 0.52	1.17± 0.32
Tumor/kidney	0.06 ± 0.03	0.08 ± 0.03	0,05 ± 0.01
Tumor/muscle	18.62 ± 6.01	20.26 ± 4.86	12.88 ± 4.08
Tumor/bone	3.71 ± 0.67	4.94 ± 1.16	3.15 ± 0.74
Left/Right lobe	4.02 ± 0.65	5.49 ± 1.47	3.48 ± 0.93

Supplemental Table 3. Tumor/organs accumulation analysis of ^{89}Zr -DFO-aGal3-F(ab')₂ in thyroid orthotopic models. The tumor-to-organ ratio values were calculated from γ -counter measurements of activity accumulated in selected organs measured at 48hr after ^{89}Zr -DFO-aGal3-F(ab')₂ injection. A positive tumor/organ ratio was measured for all selected organs, except for the liver and kidneys due to metabolism and excretion of the tracer. The positive ratio tumor/muscle indicate a high *in vivo* stability of the tracer, with very low free ^{89}Zr present in circulation and consequent low bone uptake. A high ratio left/right thyroid lobe was measured for all models investigated. Data are expressed as mean %ID/g ± SD.